

# 2D/3D Heterostructure for Semitransparent Perovskite Solar Cells with Engineered Bandgap Enables Efficiencies Exceeding 25% in Four-Terminal Tandems with Silicon and CIGS

Saba Gharibzadeh, Ihtez M. Hossain, Paul Fassl,\* Bahram Abdollahi Nejang, Tobias Abzieher, Moritz Schultes, Erik Ahlswede, Philip Jackson, Michael Powalla, Sören Schäfer, Michael Rienäcker, Tobias Wietler, Robby Peibst, Uli Lemmer, Bryce S. Richards, and Ulrich W. Paetzold\*

Wide-bandgap perovskite solar cells (PSCs) with optimal bandgap ( $E_g$ ) and high power conversion efficiency (PCE) are key to high-performance perovskite-based tandem photovoltaics. A 2D/3D perovskite heterostructure passivation is employed for double-cation wide-bandgap PSCs with engineered bandgap ( $1.65 \text{ eV} \leq E_g \leq 1.85 \text{ eV}$ ), which results in improved stabilized PCEs and a strong enhancement in open-circuit voltages of around 45 mV compared to reference devices for all investigated bandgaps. Making use of this strategy, semitransparent PSCs with engineered bandgap are developed, which show stabilized PCEs of up to 25.7% and 25.0% in four-terminal perovskite/c-Si and perovskite/CIGS tandem solar cells, respectively. Moreover, comparable tandem PCEs are observed for a broad range of perovskite bandgaps. For the first time, the robustness of the four-terminal tandem configuration with respect to variations in the perovskite bandgap for two state-of-the-art bottom solar cells is experimentally validated.


the iodide to bromide ( $X = I_{1-\gamma}\text{Br}_\gamma$ ,  $0 \leq \gamma \leq 1$ ) or cation ratio in the crystal structure.<sup>[1–3]</sup> The high power conversion efficiencies (PCEs) of perovskite solar cells (PSCs) combined with the ability to engineer the bandgap make this class of materials an excellent candidate for the wide-bandgap top absorber layer in low-cost tandem solar cells.<sup>[4–7]</sup> Simulations promise PCEs of >33% when combining wide-bandgap PSCs with established low-bandgap photovoltaic technologies such as crystalline silicon (c-Si) or copper indium gallium diselenide (CIGS) in a tandem configuration,<sup>[8–14]</sup> which is well above even the theoretical efficiency limit of market-dominating single-junction c-Si solar cells (29.6%),<sup>[15]</sup> promising to further reduce the leveled cost of electricity of photovoltaics.<sup>[16]</sup>

## 1. Introduction

Hybrid organic-inorganic lead halide perovskite semiconductors with the chemical formula  $\text{APbX}_3$ —where A is a large cation (e.g., methylammonium (MA), formamidinium (FA), and/or Cs) and X is a halogen anion (e.g., I and/or Br)—exhibit a continuously tunable bandgap ( $E_g$ ) from 1.5 to 2.3 eV by simply varying

Perovskite-based tandem solar cells combine a wide-bandgap semitransparent perovskite top solar cell that absorbs the high-energy photons with a low-bandgap bottom solar cell that absorbs the transmitted low-energy photons in different configurations. In the two-terminal (2T) configuration, both solar cells are monolithically integrated, while in the four-terminal (4T) configuration the two cells are mechanically stacked, each offering its distinct

S. Gharibzadeh, I. M. Hossain, Dr. P. Fassl, Dr. B. A. Nejang, Prof. U. Lemmer, Prof. B. S. Richards, Dr. U. W. Paetzold  
Institute of Microstructure Technology  
Karlsruhe Institute of Technology  
Hermann-von Helmholtz-Platz 1, 76344 Eggenstein-Leopoldshafen, Germany  
E-mail: paul.fassl@kit.edu; ulrich.paetzold@kit.edu

 The ORCID identification number(s) for the author(s) of this article can be found under <https://doi.org/10.1002/adfm.201909919>.

© 2020 The Authors. Published by WILEY-VCH Verlag GmbH & Co. KGaA, Weinheim. This is an open access article under the terms of the Creative Commons Attribution License, which permits use, distribution and reproduction in any medium, provided the original work is properly cited.

DOI: 10.1002/adfm.201909919

S. Gharibzadeh, I. M. Hossain, Dr. P. Fassl, Dr. B. A. Nejang, Dr. T. Abzieher, Prof. U. Lemmer, Prof. B. S. Richards, Dr. U. W. Paetzold  
Light Technology Institute  
Karlsruhe Institute of Technology  
Engesserstrasse 13, 76131 Karlsruhe, Germany  
Dr. M. Schultes, Dr. E. Ahlswede, Dr. P. Jackson, Prof. M. Powalla  
Zentrum für Sonnenenergie- und Wasserstoff-Forschung  
Baden-Württemberg (ZSW)  
Meitnerstr. 1, 70563 Stuttgart, Germany  
Dr. S. Schäfer, M. Rienäcker, Prof. T. Wietler, Prof. R. Peibst  
Institute for Solar Energy Research Hamelin (ISFH)  
Am Ohrberg 1, 31860 Emmerthal, Germany  
Prof. R. Peibst  
Institute of Electronic Materials and Devices  
Leibniz Universität Hannover  
Schneiderberg 32, 30167 Hannover, Germany

advantages and disadvantages.<sup>[7,9,17–19]</sup> The 2T architecture bears the advantage of requiring only one transparent conductive oxide (TCO) layer which induces parasitic losses. However, it also implies a series connection of both subcells,<sup>[20]</sup> which requires the development of a recombination or tunnel junction as well as current matching to maximize the PCE and, in turn, limits the bandgap combinations.<sup>[5,7]</sup> For example, c-Si bottom cells ( $E_g \approx 1.1$  eV) require a perovskite top cell with  $E_g \approx 1.73$  eV and optimized absorber thickness for optimal energy harvesting.<sup>[10,19,21,22]</sup> In addition, conformal coating of the various thin-films in the device stack of PSCs with thickness  $< 1 \mu\text{m}$  on top of commercially available textured c-Si or rough CIGS substrates is required, which poses a major challenge for fabrication.<sup>[17,23–27]</sup> In contrast, in the 4T configuration each subcell can be operated independently at its maximum power point (MPP), which allows process simplicity and reduces the constraints on top cell bandgap and thickness. When combined with c-Si bottom cells, high tandem PCEs are generally achievable with a broad range of perovskite bandgaps around  $(1.8 \pm 0.2)$  eV.<sup>[4,5,21]</sup> At the same time, this configuration requires an additional inverter, or voltage-matching of the subcells to obtain a voltage-matched 2T-module,<sup>[28]</sup> and it is harder to minimize parasitic absorption and reflectance losses (e.g., caused by additional TCOs, charge transport and optical spacer layers).<sup>[17]</sup> A three-terminal (3T) configuration could combine the advantages of monolithic integration (low parasitic absorption) and independent operation at the MPP (no current matching required),<sup>[29]</sup> potentially outperforming the 2T and 4T configurations.<sup>[30,31]</sup> A first experimental proof-of-concept of 3T perovskite/c-Si tandem solar cells has only recently been reported.<sup>[31]</sup> It should be noted that the above mentioned interrelations are not only relevant for the PCE, but also for the energy yield under realistic solar irradiation conditions.<sup>[9,32,33]</sup> Energy yield modeling confirms the minor constraints of the top cell bandgap in the 4T configuration,<sup>[8,11,32]</sup> however, no detailed experimental examination employing real prototype 4T tandem solar cells with different bottom cells has been performed so far.

To date, the most efficient perovskite-based tandem solar cells have been realized using PSCs on top of low-bandgap c-Si<sup>[6,18,21,23,25,34–42,43]</sup> or thin-film CIGS ( $E_g \approx 1.0$ – $1.2$  eV)<sup>[24,44–49]</sup> solar cells.<sup>[4,19,20,50]</sup> Record PCEs of up to 29.1% (perovskite/c-Si, 2T),<sup>[6]</sup> 27.7% (perovskite/c-Si, 4T),<sup>[43,51]</sup> 23.3% (perovskite/CIGS, 2T),<sup>[48]</sup> and 25.9% (perovskite/CIGS, 4T)<sup>[45]</sup> have been reported for the different architectures and configurations. The strong contrast between simulated ( $\approx 33\%$ ) and experimental tandem device performance is mainly due to various optical and electrical losses that reduce the PCE of today's prototype tandem solar cells.<sup>[4,10,17,52,53]</sup> These losses encompass: i) optical losses, that is, reflection at the various interfaces<sup>[17]</sup> and reduced transmission of the top cell due to parasitic absorption in the near-infrared (NIR) region within the layers;<sup>[49,54,55]</sup> and ii) electrical losses such as recombination losses, for example, non-radiative trap-assisted recombination, and imperfect contact properties.<sup>[18,19,53,55]</sup>

Various strategies to reduce optical losses in tandem solar cells have already been suggested,<sup>[17]</sup> including optimization of the thicknesses and optical properties of the various layers<sup>[12,14,53,56–59]</sup> as well as implementation of additional layers,<sup>[59,60]</sup> micro- and nanotextures, textured foils, and anti-reflection coatings.<sup>[9,53,58,59,61–67]</sup> Unfortunately, despite significant advances in developing phase-stable and high-efficiency

wide-bandgap PSCs with  $E_g > 1.7$  eV (APbI<sub>1-y</sub>Br<sub>y</sub>,  $y > \approx 0.3$ ) in recent years,<sup>[68–72]</sup> these Br-rich perovskite compositions suffer from severe recombination losses.<sup>[3,52,69,73,74]</sup> A common issue is photo-induced phase segregation and subsequent funneling of charge carriers into iodide-rich lower bandgap regions,<sup>[75]</sup> acting as radiative recombination centers.<sup>[68,69,74–80]</sup> In addition, a higher density of defect states<sup>[41,79,81,82]</sup> and stronger interfacial recombination (e.g., due to energy level offsets)<sup>[51,79,83–87]</sup> have been proposed to increase non-radiative recombination losses. Finally, the concentration of vacancy defects and strength of phase segregation seem to be directly linked to each other.<sup>[72,74,79,80,88–90]</sup> All these factors result in a larger open-circuit-voltage ( $V_{OC}$ ) deficit (defined by  $E_g/q - V_{OC}$ ) for wide-bandgap PSCs ( $> \approx 0.5$  V) as compared to state-of-the-art low-bandgap PSCs ( $\approx 0.35$ – $0.4$  V), negating a linear increase of  $V_{OC}$  with increasing bandgap.<sup>[3,52]</sup> We would like to stress that the relative contribution of the above mentioned factors to the  $V_{OC}$  deficit is a complicated function of the exact perovskite composition,<sup>[69,72,91]</sup> film surface nature,<sup>[78,84,90]</sup> defect density as well as the charge extraction layers employed.<sup>[79,86,87]</sup> One popular approach to reduce the  $V_{OC}$  deficit is to deposit a large organic cation on the surface of a 3D perovskite film, which acts as a 2D passivation agent and/or improves the energetic alignment with the charge transport layer.<sup>[92–100]</sup> In this regard, we have recently developed a novel 2D/3D perovskite heterostructure fabricated by spin-coating *n*-butylammonium bromide (BABr) on top of a wide-bandgap double-cation perovskite absorber with  $E_g \approx 1.74$  eV (FA<sub>0.83</sub>CS<sub>0.17</sub>Pb(I<sub>0.6</sub>Br<sub>0.4</sub>)<sub>3</sub>), resulting in a record  $V_{OC}$  of up to 1.31 V for this bandgap and an improved stabilized PCE of up to 19.4%.<sup>[101]</sup>

In this work, we build on the previously demonstrated high-performance wide-bandgap PSCs with 2D/3D perovskite heterostructure and employ them in a 4T tandem configuration in combination with high-efficiency c-Si and CIGS bottom solar cells. We engineer the bandgap of the perovskite top solar cell to identify the best configuration for the 4T prototype devices. Irrespective of the bandgap of the double-cation perovskite absorber, PSCs with 2D/3D heterostructure exhibit reduced non-radiative recombination losses, leading to greatly enhanced open-circuit voltages and PCEs. Finally, mechanically stacked 4T perovskite/c-Si and perovskite/CIGS tandem solar cells reach high efficiencies over a broad range of perovskite bandgaps with champion stabilized PCEs of 25.7% and 25.0%, respectively.

## 2. Results and Discussion

### 2.1. Material Properties of 2D/3D Perovskite Heterostructure and Photovoltaic Performance of Perovskite Solar Cells with Engineered Bandgap

First, we demonstrate that our recently published strategy to enhance the performance of wide-bandgap double-cation PSCs with a 2D/3D heterostructure, which is processed by spin-coating BABr dissolved in isopropanol ( $2 \text{ mg mL}^{-1}$ ) on top of the perovskite absorber layer,<sup>[101]</sup> is compatible with a broad range of perovskite bandgaps. Five different bandgaps of bulk 3D perovskite (FA<sub>0.83</sub>CS<sub>0.17</sub>Pb(I<sub>1-y</sub>Br<sub>y</sub>)<sub>3</sub>) are studied by varying the amount of bromide ( $0.24 \leq y \leq 0.56$ ) in the precursor

solution, resulting in a bandgap shift from  $\approx 1.65$  eV ( $\gamma = 0.24$ ) to  $\approx 1.85$  eV ( $\gamma = 0.56$ ) with steps of  $\Delta E_g \approx 0.05$  eV (see Tauc plots and UV-vis absorbance spectra in Figure S1, Supporting Information). X-ray diffraction (XRD) patterns of bulk 3D perovskite exhibit a shift toward larger diffraction angles with increasing bandgap due to the increased Br content in the films which results in a lattice contraction (Figure S2, Supporting Information).<sup>[2]</sup> The 3D XRD patterns are unchanged upon spin-coating BABr on top, however, consistent with our previous work new diffraction peaks at  $2\theta \approx 4.5^\circ$  and  $\approx 9^\circ$  are observed, resulting from a very thin 2D Ruddlesden-Popper (2D-RP) film formed on top of the double-cation perovskite films.<sup>[101]</sup> This interpretation is further supported by top-view scanning electron microscopy (SEM) images, which reveal a slight modification of the surface texture of perovskite films with 2D/3D heterostructure for all bandgaps (Figure S3, Supporting Information). Such a surface texture has also recently been observed in another study in which a different large cation (FEAI) was used for surface treatment.<sup>[94]</sup>

In order to investigate the effect of the 2D/3D heterostructure on the photovoltaic parameters, opaque PSCs in planar *n-i-p* architecture and the layer stack glass/ITO/nanoparticle-based  $\text{SnO}_2$  (np- $\text{SnO}_2$ )/ $\text{FA}_{0.83}\text{Cs}_{0.17}\text{Pb}(\text{I}_{1-\gamma}\text{Br}_\gamma)_3/2,2',7,7'$ -tetrakis (*N*, *N'*-di-*p*-methoxy phenylamine)-9,9'-spirobifluorene (spiro-MeOTAD)/Au with and without 2D/3D heterostructure are fabricated. The  $V_{\text{OC}}$  of the 3D reference devices increases linearly from 1.13 to 1.22 V in the bandgap range from 1.65 to 1.74 eV, however, with further increased bandgap a saturation and subsequent reduction of  $V_{\text{OC}}$  is observed (Figure 1a). The enhanced  $V_{\text{OC}}$  deficit in PSCs employing high bromide contents is commonly observed in literature and attributed to increased recombination losses in wide-bandgap PSCs.<sup>[3,51,52,75,79,81]</sup> Impressively, PSCs with 2D/3D heterostructure demonstrate an enhancement in  $V_{\text{OC}}$  of  $\approx 45$  mV for all studied bandgaps compared to the 3D reference devices (Figure 1a). We mainly attribute this enhancement to reduced non-radiative recombination losses by formation of a 2D-RP interlayer, which passivates the surface of the 3D double-cation perovskite layer.<sup>[94,99,101]</sup> Furthermore, the widening of the bandgap at the film surface due to

the 2D material with a wider bandgap might lead to a better energetic alignment with the charge transport layer and hence reduced interfacial recombination,<sup>[87]</sup> as proposed by several recent studies.<sup>[83,92,100–103]</sup> However, a detailed experimental analysis of all these factors is beyond the scope of the current work. Importantly, the relative enhancement in  $V_{\text{OC}}$  and PCE is independent of the perovskite absorber bandgap and to our knowledge this is the first time an effective 2D passivation approach is reported over such a broad bandgap range, yielding open-circuit voltages among the highest reported so far in this bandgap region. In Figure S4 and Table S1, Supporting Information, we provide a detailed literature analysis of reported champion open-circuit voltages and the corresponding  $V_{\text{OC}}$  deficits (the bandgap was determined based on EQE data provided in the manuscripts for a meaningful comparison,<sup>[104]</sup> see caption of Figure S4, Supporting Information) for  $1.53$  eV  $\leq E_g \leq 1.87$  eV and encourage other researchers to use the provided data for future comparisons. As a result, devices with 2D/3D heterostructure exhibit a significant improvement in PCE compared to the 3D reference PSCs (Figure 1b). The *J-V* characteristics and photovoltaic parameters of the corresponding PSCs show that all devices exhibit a low hysteresis between reverse and forward scan (Figure S5, Supporting Information). The best-performing solar cell using an absorber with  $E_g \approx 1.65$  eV achieves a PCE of 19.2% in the reverse current density-voltage (*J-V*) scan under air-mass 1.5 global (AM 1.5G) solar illumination. Furthermore, all PSCs deliver high stabilized PCEs of up to 17.9%, 17.6%, 17.2%, 15.6%, and 13.8% with increasing bandgap from 1.65 to 1.85 eV after 5 min of constant illumination at a constant voltage close to the MPP (Figure 1c). The stronger reduction in PCE for  $E_g > 1.74$  eV is mainly due to a larger  $V_{\text{OC}}$  deficit as already discussed.

## 2.2. 2D/3D Perovskite Heterostructure for Semitransparent Perovskite Solar Cells

In view of the remarkable performance enhancements demonstrated for various bandgaps of double-cation

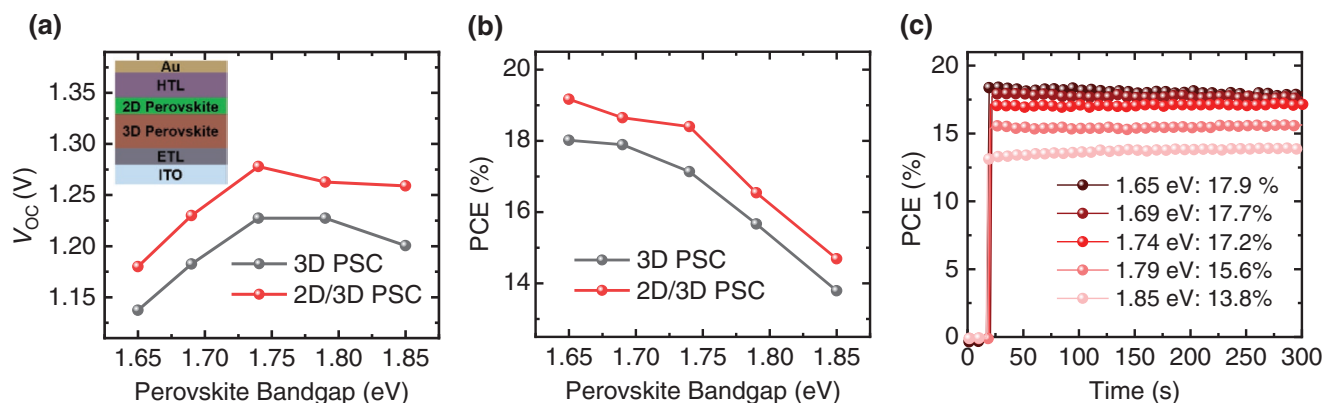


**Figure 1.** Champion device data. a) Open-circuit voltage ( $V_{\text{OC}}$ ) as a function of the perovskite bandgap for opaque perovskite solar cells (PSCs) with the structure as shown in the inset without (black) and with (red) 2D/3D perovskite heterostructure on top of the double-cation perovskite ( $\text{FA}_{0.83}\text{Cs}_{0.17}\text{Pb}(\text{I}_{1-\gamma}\text{Br}_\gamma)_3$ ) absorber layer. b) Power conversion efficiency (PCE) of the corresponding devices in the reverse current density-voltage scan under 1 sun AM1.5G illumination. c) Stabilized PCE of PSCs with 2D/3D heterostructure after 5 min constant illumination and at constant voltage close to the maximum power point.

FA<sub>0.83</sub>CS<sub>0.17</sub>Pb(I<sub>1- $\gamma$</sub> Br)<sub>3</sub> PSCs employing the 2D/3D heterostructure, we prepared a series of semitransparent PSCs with engineered bandgap, in which a semitransparent MoO<sub>x</sub>/ITO rear electrode replaces the Au electrode (as illustrated in Figure 2a). MoO<sub>x</sub> is chosen because of good band-alignment with spiro-MeOTAD and ITO and to prevent sputter damage.<sup>[54]</sup> Although the addition of this buffer layer is usually not desired due to some parasitic absorption,<sup>[54]</sup> we observe that the average transmittance of the semitransparent PSCs is hardly affected by MoO<sub>x</sub> for energies below the bandgap of the perovskite absorbers (see Figure S6, Supporting Information). The device performance follows the same trend as the opaque devices with 2D/3D heterostructure yielding semitransparent PSCs with high V<sub>OC</sub>, low hysteresis, and champion stabilized PCEs of 17.5%, 16.5%, 15.8%, 14.4%, and 12.1% with increasing bandgap from 1.65 to 1.85 eV (see champion and statistical photovoltaic parameters and *J*-*V* characteristics in Figures S7–S9, Supporting Information). We also performed initial stability measurements for all semitransparent PSCs by measuring the PCE at a constant voltage for 60 min during continuous 1 sun illumination (Figure S10, Supporting Information). We do not observe any reduction in the PCE for  $E_g \leq 1.74$  eV over that timescale. In contrast, the PCE for semitransparent PSCs with a higher Br content (i.e.,  $\gamma = 0.48$  or 0.56;  $E_g = 1.79$  or 1.85 eV) only remains stable for a period of around 30 min and then starts to gradually decrease, which might be explained by enhanced phase segregation for these compositions.<sup>[69]</sup> To study possible degradation effects on longer timescales for  $E_g = 1.65$  eV, we tracked the PCE for this composition ( $\gamma = 0.24$ ) for 11 h (Figure S11, Supporting Information) and did not observe any degradation, revealing that phase segregation or other degradation effects do not play a significant role for this composition on the studied timescales.

The onset of the external quantum efficiency (EQE) shows a consistent shift toward shorter wavelength with increasing bandgap, resulting in more light being transmitted through the top semitransparent PSCs to reach the bottom cell in a tandem configuration (top panel of Figure 2b). In order to improve the transmission of the semitransparent PSCs, which is a critical requirement for tandem applications, MgF<sub>2</sub> is deposited as an anti-reflection coating on top of the rear ITO layer (see Figures S12 and S13, Supporting Information, for transmittance, reflectance, and absorbance of device stacks with and without MgF<sub>2</sub>). While the MgF<sub>2</sub> layer at the rear side has no effect on the *J*<sub>SC</sub> of the perovskite top solar cell (see EQE measurements with and without MgF<sub>2</sub> in Figure S14, Supporting Information), it enhances the average transmittance for energies below the bandgap of the perovskite. As a result, all semitransparent PSCs exhibit an average optical transmission of more than 70% for energies below the respective bandgap of the perovskite absorber in the long wavelength region (bottom panel of Figure 2b). To analyze the effect of the shorter effective light path in semitransparent

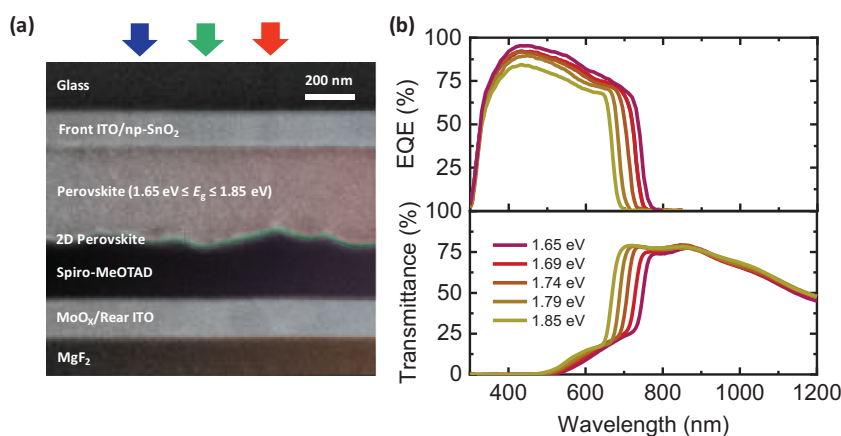


**Figure 2.** a) Cross-sectional scanning electron microscopy (SEM) image (prepared by a focused ion beam) of the semitransparent perovskite solar cells (PSCs) with 2D/3D perovskite heterostructure (the light enters from the top). b) External quantum efficiency (EQE) and transmittance of semitransparent PSCs with 2D/3D heterostructure and engineered bandgap ( $1.65 \text{ eV} \leq E_g \leq 1.85 \text{ eV}$ ).

PSCs on their *J*<sub>SC</sub> (no reflective back electrode and hence loss of the transmitted light close to the bandgap, see Figure S13, Supporting Information), in Figure S15, Supporting Information, we normalized the EQEs shown in Figure 2b to their maximum at  $\approx 430$  nm (where the transmittance is 0% for all bandgaps). In line with the absorbance measurements (Figure S13, Supporting Information), the relative EQE starts to be reduced for wavelengths above  $\approx 500$  nm for PSCs with a wider bandgap which can be ascribed to the limited absorbance closer to the perovskite bandgap. However, a slight decrease of the absolute EQE with increasing bandgap can be recognized even at wavelengths around 430 nm for which the absorbance in the perovskite absorbers is the same for all bandgaps (Figure 2b; Figure S13, Supporting Information). This effect might be ascribed to poorer charge extraction properties in Br-rich semitransparent PSCs due to energetic misalignment and/or enhanced carrier trapping,<sup>[83,84]</sup> thus, further limiting the achievable PCE for wider bandgaps.

Finally, to even better understand and compare the relevant losses in our opaque and semitransparent PSCs with engineered bandgap, we plot the champion PCE and V<sub>OC</sub> normalized to the Shockley–Queisser limit at the respective bandgaps (see Figure S16, Supporting Information). The trend for the relative V<sub>OC</sub> is very similar for opaque and semitransparent PSCs, impressively reaching its maximum value (minimum V<sub>OC</sub> deficit) for  $E_g = 1.74$  eV in both cases. In contrast, while the relative PCE for opaque devices remains similar up to  $E_g = 1.74$  eV with a subsequent drop (mainly due to the enhanced V<sub>OC</sub> deficit), semitransparent PSCs already show a decrease of the relative PCE for  $E_g > 1.65$  eV. This effect is mainly related to the additional loss in *J*<sub>SC</sub> with increasing bandgap for semitransparent PSCs as compared to opaque PSCs as discussed above.

### 2.3. High-Efficiency Four-Terminal Perovskite-Based Tandems

In line with previous reports,<sup>[38,45,46]</sup> the efficiencies of 4T tandem solar cells reported in this study are determined by mechanically

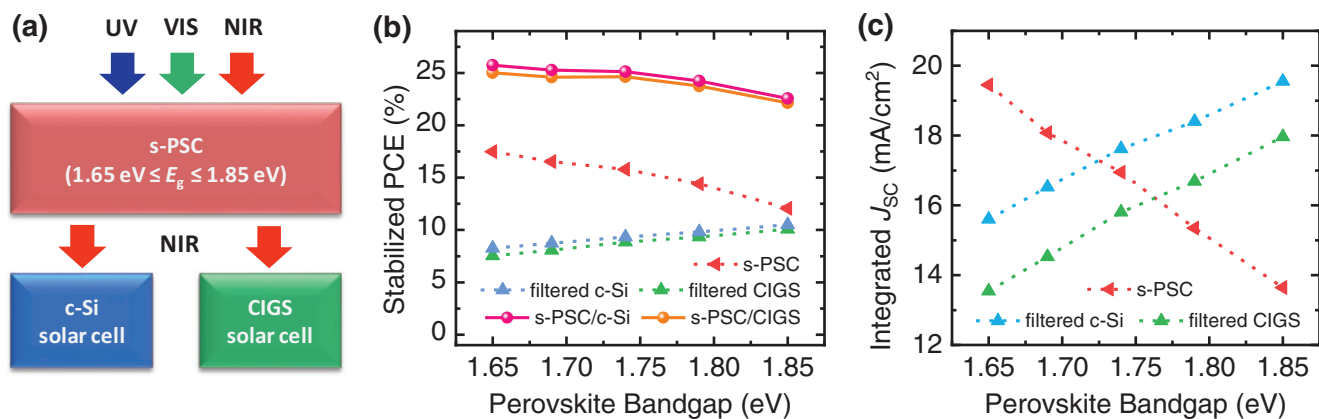


**Figure 3.** Analysis of 4T tandem solar cell configuration. a) Schematic of the 4T perovskite/c-Si or perovskite/CIGS tandem solar cell. b) Stabilized power conversion efficiency (PCE) of semitransparent perovskite solar cells (s-PSC) with 2D/3D heterostructure, filtered c-Si solar cells, filtered CIGS solar cells and s-PSC/c-Si and s-PSC/CIGS 4T tandem solar cells (calculated). c) Integrated short-circuit current density ( $J_{SC}$ ) determined from external quantum efficiency measurements of s-PSCs, filtered c-Si and filtered CIGS solar cells.

stacking semitransparent perovskite filters (substrate area 225 mm<sup>2</sup>) with the exact same structure as the semitransparent PSCs with 2D/3D heterostructure on top of highly efficient interdigitated back contact (IBC) c-Si ( $E_g \approx 1.1$  eV, PCE = 23.2%) or CIGS ( $E_g = 1.13$  eV, PCE = 21.2%) solar cells, as illustrated in **Figure 3a** (see Figures S17 and S18, Supporting Information, for schematics of the layer stack and the measurement scheme for the 4T tandem solar cells respectively). It should be noted, that the c-Si bottom solar cell suffered from perimeter losses due to the fact that we used a relatively small aperture mask for the measurements (see Experimental Section for all details), and would have a  $\approx 2\%$  absolute higher efficiency under 1 sun illumination with a fitting mask.<sup>[105]</sup> The optical properties (transmission and homogeneity) of the perovskite filters are very similar to that of the small-area semitransparent PSCs which allows us to use this method for estimating the achievable 4T tandem PCEs. In **Figure 3b** we show the stabilized PCEs of the top semitransparent PSCs (aperture area 5.6 mm<sup>2</sup>), the filtered bottom c-Si (aperture area 165 mm<sup>2</sup>) and CIGS (designated area 50 mm<sup>2</sup>) solar cells and that of the corresponding tandem solar cells (calculated by the addition of top and filtered bottom stabilized PCEs) for all investigated bandgaps. With increasing bandgap, a quasi-linear increase in the filtered PCE of the bottom c-Si and CIGS solar cells is observed in the considered energy range, which is due to the higher number of photons that are transmitted through the top semitransparent perovskite filter for wider bandgaps (**Figure 2b**), thereby enhancing the photo-generated  $J_{SC}$  in the bottom cell (**Figure 3c**). Linear fitting yields an increase in  $J_{SC}$  of 1.95 mA cm<sup>-2</sup> and 2.19 mA cm<sup>-2</sup> per 0.1 eV for the c-Si and CIGS bottom cells, respectively. However, this increase does not completely compensate for the decrease in  $J_{SC}$  with increasing bandgap of the top semitransparent PSCs, which is  $-2.86$  mA cm<sup>-2</sup> per 0.1 eV. The difference in the slopes can, in addition to the already limited EQE of semitransparent PSCs with wider bandgaps as discussed above, be explained mainly by parasitic absorption of NIR light in the oxidized spiro-MeOTAD and most importantly the rear ITO layer as well as hardly avoidable reflection losses due to interference effects (compare **Figures S12 and S13**, Supporting Information).<sup>[12,14,49,58,106,107]</sup> Therefore, the overall PCE of the

4T tandem solar cells for wider bandgaps is, in addition to the enhanced  $V_{OC}$  deficit, expected to be also limited by a stronger loss of photo-generated  $J_{SC}$  in the semitransparent PSCs as compared to its enhancement in the bottom cells. The CIGS solar cell generates  $\approx 2$  mA cm<sup>-2</sup> less  $J_{SC}$  below the bandgap of the semitransparent perovskite filters in comparison to the c-Si solar cell due to its larger bandgap and slightly reduced EQE response at longer wavelengths (**Figure S19**, Supporting Information). Along with additional currents generated in the bottom cells, their  $V_{OC}$  also slightly increases for wider bandgaps of the semitransparent perovskite filters, but only by  $\approx 3$ –4 mV per 0.1 eV given the logarithmic dependence of  $V_{OC}$  on light intensity.

The highest calculated stabilized PCEs for perovskite/c-Si and perovskite/CIGS 4T tandem solar cells reported in this study (both for  $E_g = 1.65$  eV) are 25.7% and 25.0%, respectively. Up to  $E_g \approx 1.74$  eV very similar stabilized PCEs are observed with no particular trend, which then decreases with further increasing bandgap mainly due to the limited PCE of semitransparent PSCs with  $E_g > 1.74$  eV as well as parasitic absorption of NIR light in the top cell, as discussed above in detail. The comparable tandem performance up to  $E_g = 1.74$  eV is in good agreement with detailed-balance calculations (AM1.5G illumination, 25 °C) as well as energy yield modelling (employing real weather data for the simulations) for the 4T configuration, both showing high PCEs and energy yields for a broad range of top cell bandgaps around  $(1.8 \pm 0.2)$  eV.<sup>[4,5,8,11,19,32]</sup> For comparison, in the 2T configuration only a narrow range of top cell bandgaps shows optimal PCEs and energy yields.<sup>[9,21,32]</sup> Despite the reduced stabilized PCEs for  $E_g > 1.74$  eV, our work is the first detailed experimental examination of such simulations by employing semitransparent PSCs with engineered bandgap in combination with high-efficiency c-Si and CIGS bottom solar cells in a 4T tandem configuration.

The  $J$ - $V$  characteristics and EQE responses of the champion perovskite/c-Si and perovskite/CIGS 4T tandem solar cells (both for  $E_g = 1.65$  eV) are depicted in **Figure 4**. Maximum EQEs around 70% are obtained for both c-Si and CIGS bottom cells, which is in line with the measured transmission of the semitransparent perovskite filters in the NIR region (**Figure 2b**). The photovoltaic

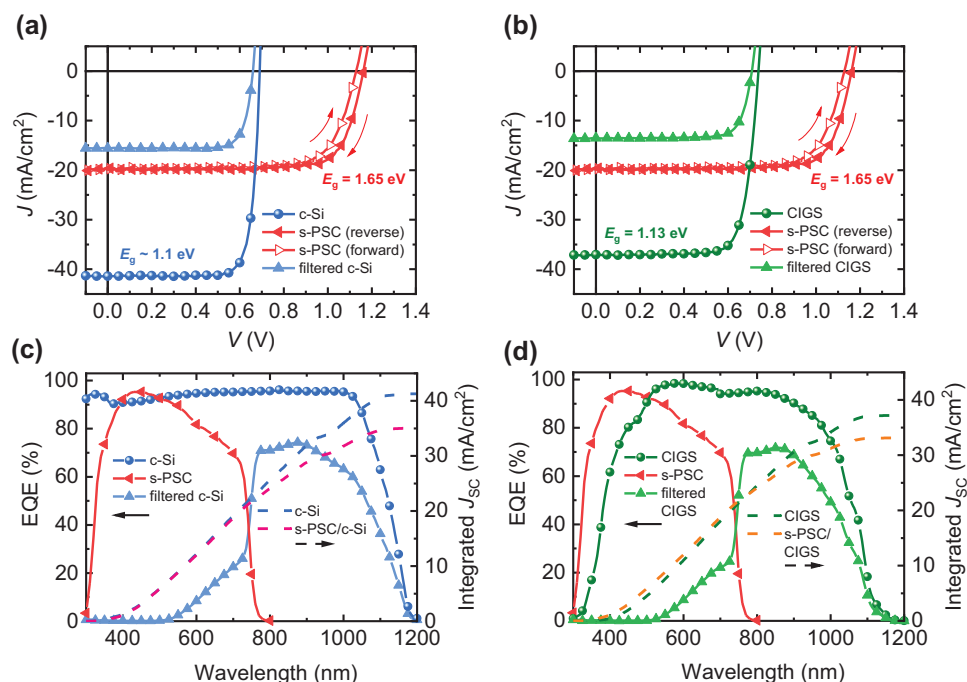


**Figure 4.** Device performance of champion 4T tandem solar cells. a,b) Current density–voltage ( $J$ – $V$ ) characteristics of semitransparent perovskite solar cells (s-PSCs) (reverse and forward scans for  $E_g = 1.65$  eV), standalone and filtered c-Si, and standalone and filtered CIGS solar cells. c,d) External quantum efficiency (EQE) of s-PSCs ( $E_g = 1.65$  eV), standalone/filtered c-Si and standalone/filtered CIGS solar cells, as well as the corresponding integrated  $J_{sc}$  of standalone and 4T tandem solar cells (sum of s-PSC and filtered c-Si/CIGS values).

parameters for the corresponding top and bottom solar cells as well as the calculated 4T tandem PCEs are summarized in **Table 1**. In comparison to the single-junction standalone c-Si or CIGS solar cells, the perovskite/Si and perovskite/CIGS 4T tandem solar cells exhibit an absolute improvement in PCE of 2.5% and 3.8%, respectively, indicating the benefit of tandem configurations over single-junction solar cells. Nevertheless, the PCEs reported here are still below feasible PCEs of perovskite-based tandems. Hence, optical losses that reduce the photo-generated charge carrier densities, both in the top and the bottom cell should be considered. For example, to reduce the reflection and transmission losses one can employ light management

schemes such as nanophotonics or interlayers,<sup>[17,60,66–67,108]</sup> as well as further improve the PSC layer stack (e.g., optimization of layer thicknesses and refractive indices and reduction of parasitic absorption).<sup>[56,57,67]</sup> This is feasible, for example, by employing a *p-i-n* structure to eliminate thick spiro-MeOTAD,<sup>[53,58,107]</sup> and more importantly by replacing the bottom and top ITO with less absorbing TCOs (which also possess a more suitable refractive index) such as indium zinc oxide (IZO), zirconium-doped indium oxide (IZRO), or hydrogen-doped indium oxide (IO:H).<sup>[14,34,49]</sup> Such improvements will further increase the overall PCE of 4T perovskite-based tandem solar cells toward 30% in the near future and are focus of our current work.

**Table 1.** Photovoltaic parameters of champion semitransparent perovskite top solar cells ( $E_g = 1.65$  eV), standalone/filtered c-Si solar cell, and standalone/filtered CIGS solar cell. The stabilized PCEs of the perovskite top and filtered bottom solar cells and the corresponding calculated 4T tandem PCEs are given in bold.

		$V_{oc}$ [V]	$J_{sc}$ [ $\text{mA cm}^{-2}$ ]	FF [%]	PCE [%]	Stabilized PCE [%]
Perovskite top solar cell ( $E_g = 1.65$ eV)	Reverse scan	1.16	19.7	78.7	18.0	<b>17.5</b>
	Forward scan	1.13	20.0	74.8	16.9	
c-Si solar cell ( $E_g \approx 1.1$ eV)	Standalone	0.69	41.4	81.2	23.2	23.2
	Filtered	0.66	15.6	80.2	8.2	<b>8.2</b>
4T perovskite/c-Si	Reverse scan				26.2	<b>25.7</b>
	Forward scan				25.1	
CIGS solar cell ( $E_g = 1.13$ eV)	Standalone	0.74	37.2	77.0	21.2	21.2
	Filtered	0.71	13.6	78.1	7.5	<b>7.5</b>
4T perovskite/CIGS	Reverse scan				25.5	<b>25.0</b>
	Forward scan				24.4	

### 3. Conclusion

In conclusion, we demonstrate double-cation PSCs with engineered bandgap ( $\text{FA}_{0.83}\text{Cs}_{0.17}\text{Pb}(\text{I}_{1-y}\text{Br}_y)_3$ ;  $0.24 \leq y \leq 0.56$ ,  $1.65 \text{ eV} \leq E_g \leq 1.85 \text{ eV}$ ) which are passivated with a 2D/3D perovskite heterostructure by spin-coating *n*-butylammonium bromide on top of the perovskite absorbers. Impressively, the 2D passivation is effective for the whole investigated bandgap range, yielding PSCs with strongly enhanced open-circuit voltages ( $\approx 45$  mV improvement) and stabilized PCEs compared to reference devices without the heterostructure. Using this strategy, champion stabilized PCEs for 4T perovskite/c-Si and perovskite/CIGS tandem solar cells of 25.7%

and 25.0% are demonstrated, respectively, corresponding to an absolute improvement of 2.5% and 3.8% with regard to the single-junction efficiencies. Our results emphasize the importance of surface passivation of the perovskite wide-bandgap top solar cell to maximize the  $V_{OC}$  and PCE. Moreover, these results are the first detailed experimental examination of the influence of the perovskite bandgap on the efficiency of 4T tandem solar cells for both, high-efficiency c-Si and CIGS bottom cells, and show that the exact bandgap is not a critical requirement for obtaining high efficiencies in this configuration.

## 4. Experimental Section

**Fabrication of Perovskite Solar Cells:** The perovskite solar cells with the layer stack glass/ITO/nanoparticle-based  $\text{SnO}_2$  (np- $\text{SnO}_2$ )/ $\text{FA}_{0.83}\text{Cs}_{0.17}\text{Pb}(\text{I}_{1-y}\text{Br}_y)_3/2,2',7,7'$ -tetrakis( $N,N'$ -di-*p*-methoxyphenylamine)-9,9'-spirobifluorene (spiro-MeOTAD)/Au were fabricated following the device fabrication process described in the earlier work.<sup>[10]</sup> The glass substrates with 120 nm thick ITO coating (sheet resistance  $15 \Omega \square^{-2}$ , Luminescence Technology, CAS: 50926-11-9) were cleaned for 10 min in an ultrasonic bath with deionized (DI) water, acetone, and isopropanol followed by 3 min of oxygen plasma treatment. A thin ( $\approx 10$  nm)  $\text{SnO}_2$  ETL was deposited on the ITO substrate by spin-coating at 4000 rpm for 30 s, followed by an annealing step at 250 °C for 30 min. The  $\text{SnO}_2$  precursor solution was prepared by diluting a 15 wt% aqueous colloidal dispersion of  $\text{SnO}_2$  nanoparticles (Alfa Aesar) in DI water to a concentration of 2.04 wt%. For preparing the 3D perovskite absorber layer ( $\approx 400$  nm thickness) with five different bandgaps ( $\text{FA}_{0.83}\text{Cs}_{0.17}\text{Pb}(\text{I}_{1-y}\text{Br}_y)_3$ ), the amount of bromide in the precursor solution was varied between  $0.24 \leq y \leq 0.56$  in steps of  $\Delta y = 0.08$ . The perovskite precursor solution was prepared by dissolving 0.83 mmol formamidinium iodide (Dyesol, CAS: 879643-71-7), 0.17 mmol CsI (Alfa Aesar, CAS: 7789-17-5),  $((2 - 3 \times y)/2)$  mmol  $\text{PbI}_2$  (Alfa Aesar, CAS: 10101-63-0), and  $(3/2 \times y)$  mmol  $\text{PbBr}_2$  (Alfa Aesar, CAS: 10031-22-8) in a 1 mL solvent mixture of  $N,N$ -dimethylformamide (Sigma Aldrich, CAS: 68-12-2):dimethylsulfoxide (Sigma Aldrich, CAS: 67-68-5) 4:1 (v:v). The double-cation perovskite absorber layer was deposited on top of  $\text{SnO}_2$  (after a short oxygen plasma treatment for 1 min) from solution using a two-step spin coating process: i) 1000 rpm for 10 s, ii) 5000 rpm for 30 s. Chlorobenzene (100  $\mu\text{L}$ , Sigma Aldrich, CAS: 108-90-7) was poured on the spinning substrate 10 s before the end of the second step. The samples were annealed at 100 °C for 30 min in inert nitrogen atmosphere. The 2D/3D heterostructure was processed by dynamically spin-coating 100  $\mu\text{L}$  of *n*-BABr (Dyesol, CAS: 15567-09-6) dissolved in isopropanol (Sigma-Aldrich, CAS: 67-63-0) at a concentration of 2 mg  $\text{mL}^{-1}$  at 5000 rpm for 30 s on top of the perovskite absorber layer with a subsequent annealing at 100 °C for 5 min in inert nitrogen atmosphere. As HTL, spiro-OMeTAD ( $\approx 220$ – $250$  nm thickness) was deposited by spin-coating at 4000 rpm for 30 s. The corresponding precursor solution contained 80 mg spiro-OMeTAD (Luminescence Technology) dissolved in 1 mL chlorobenzene with the additives 17.5  $\mu\text{L}$  lithium bis(trifluoromethanesulfonyl) imide (Sigma Aldrich, CAS: 90076-65-6) (520 mg  $\text{mL}^{-1}$  in acetonitrile) and 28.5  $\mu\text{L}$  4-tert butylpyridine (Sigma Aldrich, CAS: 3978-81-2). The samples coated with spiro-OMeTAD were exposed to dry air ( $\approx 25\%$  relative humidity) for  $\approx 12$  h before a 60 nm thick Au electrode was deposited by thermal evaporation through shadow masks to define the active area to 10.5  $\text{mm}^2$ . In the current study the  $V_{OC}$  of the champion device reported in our last work, as shown in Figure S4, Supporting Information ( $E_g \approx 1.74$  eV;  $V_{OC} \approx 1.31$  eV), could not be reproduced.<sup>[9]</sup> One important reason for that is the poorer quality of the precursor material  $\text{PbI}_2$  during the course of this study, which is the key component in fabricating highly efficient PSCs. TCI even suspended their delivery from March 2019 onward because of these quality issues (see Notes at: <https://www.tcichemicals.com/eshop/en/us/commodity/L0279/>).

The front and rear ITO (for semitransparent perovskite solar cells with active area 10.5  $\text{mm}^2$ ) were deposited using a Kurt J. Lesker PVD-75 thin-film deposition system. The following sputtering parameters were used for the front (rear) ITO: Power 50 W (50 W), substrate temperature = 300 °C (25 °C), deposition time = 2000 s (2300 s), pressure = 0.8 mTorr (0.8 mTorr),  $\text{O}_2$  to argon ratio = 3.5% (2.5%), and thickness  $\approx 135$  nm ( $\approx 150$  nm). The sheet resistance of the deposited ITO was  $10$ – $12 \Omega \square^{-1}$  ( $40$ – $50 \Omega \square^{-1}$ ). Before the deposition of the rear ITO,  $\approx 10$  nm of  $\text{MoO}_x$  (Sigma Aldrich) was evaporated on top of spiro-MeOTAD at a rate of 0.8  $\text{Å s}^{-1}$  using a Lesker Spectros system at  $6 \times 10^{-6}$  mbar pressure. To increase the conductivity of the rear ITO,  $\approx 75$  nm Au fingers were deposited by thermal evaporation at a rate of 2  $\text{Å s}^{-1}$  using a shadow mask. As an anti-reflection coating, magnesium fluoride ( $\text{MgF}_2$ ) was deposited by thermal evaporation on top of the rear ITO using Lesker Spectros PVD system at a rate of 3–4  $\text{Å s}^{-1}$  at  $6 \times 10^{-6}$  mbar pressure. It shall be noted that using, for example, silicone or paraffin oil as an optical coupler would result in a slightly more effective suppression of multiple reflections between the top and bottom cell in a 4T tandem configuration. For the measurements of the bottom cells in a 4T configuration, semitransparent perovskite filters with the same structure and optical properties as that of the semitransparent perovskite solar cells were prepared (225  $\text{mm}^2$  substrate size).

**Fabrication of IBC Single-Junction Crystalline-Silicon (c-Si) Bottom Solar Cells:** The IBC single-junction c-Si solar cells with an designated area of 400  $\text{mm}^2$  were fabricated following the device fabrication process described in the earlier work.<sup>[109]</sup>

**Fabrication of CIGS Bottom Solar Cells:** The CIGS solar cells were fabricated by co-evaporation of the elements in a classical multistage process which is described in detail in the earlier work.<sup>[110]</sup> The cells comprised a metal grid and an anti-reflective  $\text{MgF}_2$  coating on top, the designated area was 50  $\text{mm}^2$  (defined by mechanical scribing).

**Device Characterization—Current Density–Voltage ( $J$ – $V$ ) Measurements:** The perovskite and c-Si solar cells were characterized using a class AAA Newport solar simulator (xenon lamp). For the CIGS solar cells, a class AAA Wacom WXS-90S-5, AM1.5G Super Solar Simulator (xenon lamp) was used. The solar simulator for the measurements of the perovskite solar cells was calibrated with a certified Si photodiode (Fraunhofer ISE) equipped with a KG5 band pass filter. The  $J$ – $V$  measurements were carried out under AM 1.5G conditions from open-circuit voltage ( $V_{OC}$ ) to short-circuit current density ( $J_{SC}$ ) and  $J_{SC}$  to  $V_{OC}$  at a fixed rate of 600  $\text{mV s}^{-1}$  using a Keithley 2400 source meter. The stabilized PCE of the perovskite solar cells was determined by the power output at constant voltage close to the MPP under continuous AM 1.5G illumination for 5 min. The temperature (25 °C) of the perovskite solar cells was controlled actively using a Peltier element control circuit. The opaque perovskite solar cells were measured in nitrogen atmosphere without shadow mask. The c-Si and CIGS solar cells were measured either standalone or below the semitransparent perovskite filters with different bandgaps (filtered PCE). The semitransparent perovskite and c-Si solar cells were measured in nitrogen atmosphere using aperture masks with areas of 5.6 and 165  $\text{mm}^2$ , respectively, while the CIGS solar cells were measured in ambient air without mask (designated area 50  $\text{mm}^2$ ). In Figures S17 and S18, Supporting Information, schematics of the layer stack and the 4T tandem measurement setup, respectively (bottom cell measured below perovskite filter) are provided. In order to account for spectral mismatch caused by the different bandgaps of the perovskite filters, the intensity of the solar simulator was adjusted so that the  $J_{SC}$  from the  $J$ – $V$  measurement matched the integrated  $J_{SC}$  from the EQE measurements.

**External Quantum Efficiency Measurements:** EQE measurements were performed using a Bentham EQE system. A chopping frequency of  $\approx 930$  Hz with an integration time of 500 ms was used to obtain the spectra. The devices were not subjected to any pre-conditioning. In order to average over possible slight variations in the EQE spectra of the bottom c-Si and CIGS cells when measured below the perovskite filters, which can be induced by inhomogeneous scattering and transmission properties due to typical thickness variations of double-cation  $\text{FA}_{0.83}\text{Cs}_{0.17}\text{Pb}(\text{I}_{1-y}\text{Br}_y)_3$  perovskite films (“wrinkle structure,” compare Braunger et al. and Bush et al.),<sup>[111,112]</sup> a large illumination spot was used. The absolute EQE values and hence integrated  $J_{SC}$  of the CIGS

bottom cells were corrected to account for the finger lines of the metal grid (shading effect).

**Scanning Electron Microscopy (SEM):** Focused ion beam (FIB) assisted SEM was performed using a Zeiss Crossbeam 1540 EsB scanning electron microscope. A FIB with a gallium source was used for creating a cut through the entire sample. 1–2 keV was typically used for capturing an image. The top view SEM images were taken with Zeiss LEO1530 microscope having an in-lens detector and an aperture size of 20 μm.

**UV-Vis Spectrophotometry:** The transmittance and reflectance measurements were performed using a PerkinElmer Lambda 1050 spectrophotometer employed with an integrating sphere. The illumination spot was set as large as possible to average over possible slight inhomogeneities of the films.

**X-Ray Diffraction:** The crystal structure of perovskite layers for different bandgaps were examined by XRD (D2Phaser – Bruker) with Cu Kα radiation ( $\lambda = 1.5405 \text{ \AA}$ ) in Bragg–Brentano configuration using a LynxEye detector. The measurements were performed on unfinished device stacks with the same layer sequence as the perovskite solar cells, that is, glass/ITO/np-SnO<sub>2</sub>/FA<sub>0.83</sub>Cs<sub>0.17</sub>Pb(1–*y*Br)<sub>3</sub>.

## Supporting Information

Supporting Information is available from the Wiley Online Library or from the author.

## Acknowledgements

S.G. and I.M.H. contributed equally to this work. The authors acknowledge the financial supports by the Initiating and Networking funding of the Helmholtz Association (HYIG of Dr. U.W. Paetzold [VH-NG-1148]; Recruitment Initiative of Prof. B.S. Richards; the Helmholtz Energy Materials Foundry (HEMF); PEROSEED [ZT-0024]; Innovationpool); the Helmholtz Association – through the program “Science and Technology of Nanosystems (STN)”; the KIT Young Investigator Network; the German Federal Ministry for Economic Affairs (BMWi) (grant: CAPITANO [03EE1038B]); and the German Federal Ministry of Education and Research (BMBF) (grant: PRINTPERO [03SF0557A]). The authors gratefully acknowledge the help and support of the Karlsruhe School of Optics & Photonics (KSOP) and Max Planck School of Photonics (MPSP), respectively. The work at ISFH was supported by the German Federal Ministry for Economic Affairs and Energy (BMWi) under contract no. 0325827A and the State of Lower Saxony.

## Conflict of Interest

The authors declare no conflict of interest.

## Keywords

2D perovskites, 3D perovskites, copper indium gallium diselenide, tandem solar cells

Received: November 27, 2019

Revised: January 22, 2020

Published online: March 11, 2020

- [1] J. H. Noh, S. H. Im, J. H. Heo, T. N. Mandal, S. Il Seok, *Nano Lett.* **2013**, *13*, 1764.  
 [2] T. Jesper Jacobsson, J.-P. Correa-Baena, M. Pazoki, M. Saliba, K. Schenk, M. Grätzel, A. Hagfeldt, *Energy Environ. Sci.* **2016**, *9*, 1706.  
 [3] E. L. Unger, L. Kegelman, K. Suchan, D. Sörell, L. Korte, S. Albrecht, *J. Mater. Chem. A* **2017**, *5*, 11401.

- [4] T. Leijtens, K. A. Bush, R. Prasanna, M. D. McGehee, *Nat. Energy* **2018**, *3*, 828.  
 [5] G. E. Eperon, M. T. Hörantner, H. J. Snaith, *Nature Rev. Chem.* **2017**, *1*, 0095.  
 [6] NREL Best Research-Cell Efficiency Chart, <https://www.nrel.gov/pv/cell-efficiency.html>, (accessed: February 2020).  
 [7] Z. Wang, Z. Song, Y. Yan, S. (Frank) Liu, D. Yang, *Adv. Sci.* **2019**, *6*, 1801704.  
 [8] M. T. Hörantner, H. J. Snaith, *Energy Environ. Sci.* **2017**, *10*, 1983.  
 [9] J. Lehr, M. Langenhorst, R. Schmager, S. Kirner, U. Lemmer, B. S. Richards, C. Case, U. W. Paetzold, *Sustainable Energy Fuels* **2018**, *2*, 2754.  
 [10] M. T. Hörantner, T. Leijtens, M. E. Ziffer, G. E. Eperon, M. G. Christoforo, M. D. McGehee, H. J. Snaith, *ACS Energy Lett.* **2017**, *2*, 2506.  
 [11] R. Hosseinian Ahangharnejhad, A. B. Phillips, K. Ghimire, P. Koirala, Z. Song, H. M. M. Barudi, A. Habte, M. Sengupta, R. J. Ellingson, Y. Yan, R. W. Collins, N. J. Podraza, M. J. Heben, *Sustainable Energy Fuels* **2019**, *3*, 1841.  
 [12] M. Filipič, P. Löper, B. Niesen, S. De Wolf, J. Krč, C. Ballif, M. Topič, *Opt. Express* **2015**, *23*, A263.  
 [13] M. H. Futscher, B. Ehrler, *ACS Energy Lett.* **2017**, *2*, 2089.  
 [14] K. Jäger, L. Korte, B. Rech, S. Albrecht, *Opt. Express* **2017**, *25*, A473.  
 [15] S. Schafer, R. Brendel, *IEEE J. Photovoltaics* **2018**, *8*, 1156.  
 [16] Z. Li, Y. Zhao, X. Wang, Y. Sun, Z. Zhao, Y. Li, H. Zhou, Q. Chen, *Joule* **2018**, *2*, 1559.  
 [17] D. A. Jacobs, M. Langenhorst, F. Sahli, B. S. Richards, T. P. White, C. Ballif, K. R. Catchpole, U. W. Paetzold, *J. Phys. Chem. Lett.* **2019**, *10*, 3159.  
 [18] M. Jaysankar, M. Filipič, B. Zielinski, R. Schmager, W. Song, W. Qiu, U. W. Paetzold, T. Aernouts, M. Debucquoy, R. Gehlhaar, J. Poortmans, *Energy Environ. Sci.* **2018**, *11*, 1489.  
 [19] J. Werner, B. Niesen, C. Ballif, *Adv. Mater. Interfaces* **2018**, *5*, 1700731.  
 [20] C. D. Bailie, M. G. Christoforo, J. P. Mailoa, A. R. Bowring, E. L. Unger, W. H. Nguyen, J. Burschka, N. Pellet, J. Z. Lee, M. Grätzel, R. Noufi, T. Buonassisi, A. Salleo, M. D. McGehee, *Energy Environ. Sci.* **2015**, *8*, 956.  
 [21] Z. Yu, M. Leilaoui, Z. Holman, *Nat. Energy* **2016**, *1*, 16137.  
 [22] S. Rühle, *Phys. Status Solidi A* **2017**, *214*, 1600955.  
 [23] F. Sahli, J. Werner, B. A. Kamino, M. Bräuninger, R. Monnard, B. Paviet-Salomon, L. Barraud, L. Ding, J. J. Diaz Leon, D. Sacchetto, G. Cattaneo, M. Despeisse, M. Boccard, S. Nicolay, Q. Jeangros, B. Niesen, C. Ballif, *Nat. Mater.* **2018**, *17*, 820.  
 [24] M. Jošt, T. Bertram, D. Koushik, J. A. Marquez, M. A. Verheijen, M. D. Heinemann, E. Köhnen, A. Al-Ashouri, S. Braunger, F. Lang, B. Rech, T. Unold, M. Creatore, I. Laueremann, C. A. Kaufmann, R. Schlattmann, S. Albrecht, *ACS Energy Lett.* **2019**, *4*, 583.  
 [25] G. Nogat, F. Sahli, J. Werner, R. Monnard, M. Boccard, M. Despeisse, F.-J. J. Haug, Q. Jeangros, A. Ingenito, C. Ballif, *ACS Energy Lett.* **2019**, *4*, 844.  
 [26] J. Werner, F. Sahli, F. Fu, J. J. Diaz Leon, A. Walter, B. A. Kamino, B. Niesen, S. Nicolay, Q. Jeangros, C. Ballif, *ACS Energy Lett.* **2018**, *3*, 2052.  
 [27] T. Abzieher, J. A. Schwenzer, S. Moghadamzadeh, F. Sutterluti, I. M. Hossain, M. Pfau, E. Lotter, M. Hetterich, B. S. Richards, U. Lemmer, M. Powalla, U. W. Paetzold, *IEEE J. Photovoltaics* **2019**, *9*, 1249.  
 [28] S. MacAlpine, D. C. Bobela, S. Kurtz, M. P. Lumb, K. J. Schmieder, J. E. Moore, R. J. Walters, K. Alberi, *J. Photonics Energy* **2017**, *7*, 1.  
 [29] M. Rienäcker, E. L. Warren, M. Schnabel, H. Schulte-Huxel, R. Niepelt, R. Brendel, P. Stradins, A. C. Tamboli, R. Peibst, *Prog. Photovoltaics* **2019**, *27*, 410.  
 [30] E. L. Warren, M. G. Deceglie, M. Rienäcker, R. Peibst, A. C. Tamboli, P. Stradins, *Sustainable Energy Fuels* **2018**, *2*, 1141.



- [31] P. Tockhorn, P. Wagner, L. Kegelmann, J.-C. Stang, M. Mews, S. Albrecht, L. Korte, *ACS Appl. Energy Mater.* **2020**, <https://doi.org/10.1021/acsaem.9b01800>.
- [32] M. Langenhorst, B. Sautter, R. Schmager, J. Lehr, E. Ahlswede, M. Powalla, U. Lemmer, B. S. Richards, U. W. Paetzold, *Prog. Photovoltaics* **2019**, *27*, 290.
- [33] R. Schmager, M. Langenhorst, J. Lehr, U. Lemmer, B. S. Richards, U. W. Paetzold, *Opt. Express* **2019**, *27*, A507.
- [34] E. Aydin, M. De Bastiani, X. Yang, M. Sajjad, F. Aljamaan, Y. Smirnov, M. N. Hedhili, W. Liu, T. G. Allen, L. Xu, E. Van Kerschaver, M. Morales-Masis, U. Schwingenschlögl, S. De Wolf, *Adv. Funct. Mater.* **2019**, *29*, 1901741.
- [35] Z. Wang, X. Zhu, S. Zuo, M. Chen, C. Zhang, C. Wang, X. Ren, Z. Yang, Z. Liu, X. Xu, Q. Chang, S. Yang, F. Meng, Z. Liu, N. Yuan, J. Ding, S. (Frank) Liu, D. Yang, *Adv. Funct. Mater.* **2020**, *30*, 1908298.
- [36] C. O. Ramírez Quiroz, G. D. Spyropoulos, M. Salvador, L. M. Roch, M. Berlinghof, J. Darío Perea, K. Forberich, L. Dion-Bertrand, N. J. Schrenker, A. Classen, N. Gasparini, G. Chistiakova, M. Mews, L. Korte, B. Rech, N. Li, F. Hauke, E. Spiecker, T. Ameri, S. Albrecht, G. Abellán, S. León, T. Unruh, A. Hirsch, A. Aspuru-Guzik, C. J. Brabec, *Adv. Funct. Mater.* **2019**, *29*, 1901476.
- [37] J. Werner, L. Barraud, A. Walter, M. Bräuninger, F. Sahli, D. Sacchetto, N. Tétreault, B. Paviet-Salomon, S.-J. Moon, C. Allebé, M. Despeisse, S. Nicolay, S. De Wolf, B. Niesen, C. Ballif, *ACS Energy Lett.* **2016**, *1*, 474.
- [38] T. Duong, Y. Wu, H. Shen, J. Peng, X. Fu, D. Jacobs, E.-C. Wang, T. C. Kho, K. C. Fong, M. Stocks, E. Franklin, A. Blakers, N. Zin, K. McIntosh, W. Li, Y.-B. Cheng, T. P. White, K. Weber, K. Catchpole, *Adv. Energy Mater.* **2017**, *7*, 1700228.
- [39] M. Jaysankar, W. Qiu, M. van Eerden, T. Aernouts, R. Gehlhaar, M. Debuquoy, U. W. Paetzold, J. Poortmans, *Adv. Energy Mater.* **2017**, *7*, 1602807.
- [40] H. A. Dewi, H. Wang, J. Li, M. Thway, R. Sridharan, R. Stangl, F. Lin, A. G. Aberle, N. Mathews, A. Bruno, S. Mhaisalkar, *ACS Appl. Mater. Interfaces* **2019**, *11*, 34178.
- [41] B. Chen, Z. Yu, K. Liu, X. Zheng, Y. Liu, J. Shi, D. Spronk, P. N. Rudd, Z. Holman, J. Huang, *Joule* **2019**, *3*, 177.
- [42] J. Zheng, H. Mehrvarz, C. Liao, J. Bing, X. Cui, Y. Li, V. R. Gonçalves, C. F. J. Lau, D. S. Lee, Y. Li, M. Zhang, J. Kim, Y. Cho, L. G. Caro, S. Tang, C. Chen, S. Huang, A. W. Y. Ho-Baillie, *ACS Energy Lett.* **2019**, *4*, 2623.
- [43] T. Duong, H. Pham, T. C. Kho, P. Phang, K. C. Fong, D. Yan, Y. Yin, J. Peng, M. A. Mahmud, S. Gharibzadeh, B. A. Nejad, I. M. Hossain, M. R. Khan, N. Mozaffari, Y. Wu, H. Shen, J. Zheng, H. Mai, W. Liang, C. Samundsett, M. Stocks, K. McIntosh, G. G. Andersson, U. Lemmer, B. S. Richards, U. W. Paetzold, A. Ho-Baillie, Y. Liu, D. Macdonald, A. Blakers, J. Wong-Leung, T. White, K. Weber, K. Catchpole, *Adv. Energy Mater.* **2020**, <https://doi.org/10.1002/aem.201903553>.
- [44] Q. Han, Y. Hsieh, L. Meng, J. Wu, P. Sun, E. Yao, S. Chang, S. Bae, T. Kato, V. Bermudez, Y. Yang, *Science* **2018**, *361*, 904.
- [45] D. H. Kim, C. P. Muzzillo, J. Tong, A. F. Palmstrom, B. W. Larson, C. Choi, S. P. Harvey, S. Glynn, J. B. Whitaker, F. Zhang, Z. Li, H. Lu, M. F. A. M. van Hest, J. J. Berry, L. M. Mansfield, Y. Huang, Y. Yan, K. Zhu, *Joule* **2019**, *3*, 1734.
- [46] H. Shen, T. Duong, J. Peng, D. Jacobs, N. Wu, J. Gong, Y. Wu, S. K. Karuturi, X. Fu, K. Weber, X. Xiao, T. P. White, K. Catchpole, *Energy Environ. Sci.* **2018**, *11*, 394.
- [47] U. W. Paetzold, M. Jaysankar, R. Gehlhaar, E. Ahlswede, S. Paetel, W. Qiu, J. Bastos, L. Rakocevic, B. S. Richards, T. Aernouts, M. Powalla, J. Poortmans, *J. Mater. Chem. A* **2017**, *5*, 9897.
- [48] A. Al-Ashouri, A. Magomedov, M. Roß, M. Jošt, M. Talaikis, G. Chistiakova, T. Bertram, J. A. Márquez, E. Köhnen, E. Kasparavičius, S. Levenco, L. Gil-Escrig, C. J. Hages, R. Schlatmann, B. Rech, T. Malinauskas, T. Unold, C. A. Kaufmann, L. Korte, G. Niaura, V. Getautis, S. Albrecht, *Energy Environ. Sci.* **2019**, *12*, 3356.
- [49] M. Schultes, T. Helder, E. Ahlswede, M. F. Aygüler, P. Jackson, S. Paetel, J. A. Schwenzer, I. M. Hossain, U. W. Paetzold, M. Powalla, *ACS Appl. Energy Mater.* **2019**, *2*, 7823.
- [50] M. Jaysankar, S. Paetel, E. Ahlswede, U. W. Paetzold, T. Aernouts, R. Gehlhaar, J. Poortmans, *Prog. Photovoltaics Res. Appl.* **2019**, *27*, 733.
- [51] M. Jaysankar, B. A. L. Raul, J. Bastos, C. Burgess, C. Weijtens, M. Creatore, T. Aernouts, Y. Kuang, R. Gehlhaar, A. Hadipour, J. Poortmans, *ACS Energy Lett.* **2019**, *4*, 259.
- [52] T. C.-J. Yang, P. Fiala, Q. Jeangros, C. Ballif, *Joule* **2018**, *2*, 1421.
- [53] K. A. Bush, S. Manzoor, K. Frohna, Z. J. Yu, J. A. Raiford, A. F. Palmstrom, H. P. Wang, R. Prasanna, S. F. Bent, Z. C. Holman, M. D. McGehee, *ACS Energy Lett.* **2018**, *3*, 2173.
- [54] T. Duong, N. Lal, D. Grant, D. Jacobs, P. Zheng, S. Rahman, H. Shen, M. Stocks, A. Blakers, K. Weber, T. P. White, K. R. Catchpole, *IEEE J. Photovoltaics* **2016**, *6*, 679.
- [55] C. O. Ramírez Quiroz, Y. Shen, M. Salvador, K. Forberich, N. Schrenker, G. D. Spyropoulos, T. Heumüller, B. Wilkinson, T. Kirchartz, E. Spiecker, P. J. Verlinden, X. Zhang, M. A. Green, A. Ho-Baillie, C. J. Brabec, *J. Mater. Chem. A* **2018**, *6*, 3583.
- [56] S. Manzoor, J. Häusele, K. A. Bush, A. F. Palmstrom, J. Carpenter, Z. J. Yu, S. F. Bent, M. D. McGehee, Z. C. Holman, *Opt. Express* **2018**, *26*, 27441.
- [57] M. Koç, W. Soltanpoor, G. Bektaş, H. J. Bolink, S. Yerci, *Adv. Opt. Mater.* **2019**, *7*, 1900944.
- [58] S. Altazin, L. Stepanova, J. Werner, B. Niesen, C. Ballif, B. Ruhstaller, *Opt. Express* **2018**, *26*, A579.
- [59] M. Werth, R. Schlatmann, L. Mazzarella, S. Albrecht, K. Jäger, M. Jošt, B. Stannowski, L. Korte, *Opt. Express* **2018**, *26*, A487.
- [60] K. Bittkau, T. Kirchartz, U. Rau, *Opt. Express* **2018**, *26*, A750.
- [61] R. Santbergen, R. Mishima, T. Meguro, M. Hino, H. Uzu, J. Blanker, K. Yamamoto, M. Zeman, *Opt. Express* **2016**, *24*, A1288.
- [62] U. W. Paetzold, W. Qiu, F. Finger, J. Poortmans, D. Cheyons, *Appl. Phys. Lett.* **2015**, *106*, 173101.
- [63] M. Jošt, E. Köhnen, A. B. Morales-Vilches, B. Lipovšek, K. Jäger, B. Macco, A. Al-Ashouri, J. Krč, L. Korte, B. Rech, R. Schlatmann, M. Topič, B. Stannowski, S. Albrecht, *Energy Environ. Sci.* **2018**, *11*, 3511.
- [64] F. Hou, C. Han, O. Isabella, L. Yan, B. Shi, J. Chen, S. An, Z. Zhou, W. Huang, H. Ren, Q. Huang, G. Hou, X. Chen, Y. Li, Y. Ding, G. Wang, C. Wei, D. Zhang, M. Zeman, Y. Zhao, X. Zhang, *Nano Energy* **2019**, *56*, 234.
- [65] R. Schmager, G. Gomard, B. S. Richards, U. W. Paetzold, *Sol. Energy Mater. Sol. Cells* **2019**, *192*, 65.
- [66] D. Chen, P. Manley, *J. Photonics Energy* **2018**, *8*, 1.
- [67] K. Li, S. Zhang, Y. Ruan, D. Li, T. Zhang, H. Zhen, *Opt. Express* **2019**, *27*, A1004.
- [68] D. P. McMeekin, G. Sadoughi, W. Rehman, G. E. Eperon, M. Saliba, M. T. Horantner, A. Haghighirad, N. Sakai, L. Korte, B. Rech, M. B. Johnston, L. M. Herz, H. J. Snaith, *Science* **2016**, *351*, 151.
- [69] K. A. Bush, K. Frohna, R. Prasanna, R. E. Beal, T. Leijtens, S. A. Swifter, M. D. McGehee, *ACS Energy Lett.* **2018**, *3*, 428.
- [70] A. Rajagopal, R. J. Stoddard, S. B. Jo, H. W. Hillhouse, A. K. Y. Jen, *Nano Lett.* **2018**, *18*, 3985.
- [71] W. Rehman, D. P. McMeekin, J. B. Patel, R. L. Milot, M. B. Johnston, H. J. Snaith, L. M. Herz, *Energy Environ. Sci.* **2017**, *10*, 361.
- [72] Y. Zhou, Y.-H. Jia, H.-H. Fang, M. A. Loi, F.-Y. Xie, L. Gong, M.-C. Qin, X.-H. Lu, C.-P. Wong, N. Zhao, *Adv. Funct. Mater.* **2018**, *28*, 1803130.

- [73] Y. Luo, S. Aharon, M. Stuckelberger, E. Magaña, B. Lai, M. I. Bertoni, L. Etgar, D. P. Fenning, *Adv. Funct. Mater.* **2018**, *28*, 1706995.
- [74] A. J. Barker, A. Sadhanala, F. Deschler, M. Gandini, S. P. Senanayak, P. M. Pearce, E. Mosconi, A. J. Pearson, Y. Wu, A. R. Srimath Kandada, T. Leijtens, F. De Angelis, S. E. Dutton, A. Petrozza, R. H. Friend, *ACS Energy Lett.* **2017**, *2*, 1416.
- [75] E. T. Hoke, D. J. Slotcavage, E. R. Dohner, A. R. Bowring, H. I. Karunadasa, M. D. McGehee, *Chem. Sci.* **2015**, *6*, 613.
- [76] D. J. Slotcavage, H. I. Karunadasa, M. D. McGehee, *ACS Energy Lett.* **2016**, *1*, 1199.
- [77] D. Forgács, D. Pérez-del-Rey, J. Ávila, C. Momblona, L. Gil-Escrig, B. Dänekamp, M. Sessolo, H. J. Bolink, *J. Mater. Chem. A* **2017**, *5*, 3203.
- [78] Z. Andaji-Garmaroudi, M. Abdi-Jalebi, D. Guo, S. Macpherson, A. Sadhanala, E. M. Tennyson, E. Ruggeri, M. Anaya, K. Galkowski, R. Shivanna, K. Lohmann, K. Frohna, S. Mackowski, T. J. Savenije, R. H. Friend, S. D. Stranks, *Adv. Mater.* **2019**, *31*, 1902374.
- [79] S. Mahesh, J. M. Ball, R. D. J. Oliver, D. P. McMeekin, P. Nayak, M. B. Johnston, H. Snaith, *Energy Environ. Sci.* **2019**, *50*, 675.
- [80] A. J. Knight, A. D. Wright, J. B. Patel, D. P. McMeekin, H. J. Snaith, M. B. Johnston, L. M. Herz, *ACS Energy Lett.* **2019**, *4*, 75.
- [81] I. Levine, O. G. Vera, M. Kulbak, D.-R. Ceratti, C. Rehermann, J. A. Márquez, S. Levchenko, T. Unold, G. Hodes, I. Balberg, D. Cahen, T. Dittrich, *ACS Energy Lett.* **2019**, *4*, 1150.
- [82] H. Tan, F. Che, M. Wei, Y. Zhao, M. I. Saidaminov, P. Todorović, D. Broberg, G. Walters, F. Tan, T. Zhuang, B. Sun, Z. Liang, H. Yuan, E. Fron, J. Kim, Z. Yang, O. Voznyy, M. Asta, E. H. Sargent, *Nat. Commun.* **2018**, *9*, 3100.
- [83] Y. Lin, B. Chen, F. Zhao, X. Zheng, Y. Deng, Y. Shao, Y. Fang, Y. Bai, C. Wang, J. Huang, *Adv. Mater.* **2017**, *29*, 1700607.
- [84] R. A. Belisle, K. A. Bush, L. Bertoluzzi, A. Gold-Parker, M. F. Toney, M. D. McGehee, *ACS Energy Lett.* **2018**, *3*, 2694.
- [85] A. Zohar, M. Kulbak, I. Levine, G. Hodes, A. Kahn, D. Cahen, *ACS Energy Lett.* **2019**, *4*, 1.
- [86] D. B. Khadka, Y. Shirai, M. Yanagida, T. Noda, K. Miyano, *ACS Appl. Mater. Interfaces* **2018**, *10*, 22074.
- [87] M. Stolterfoht, P. Caprioglio, C. M. Wolff, J. A. Márquez, J. Nordmann, S. Zhang, D. Rothhardt, U. Hörmann, Y. Amir, A. Redinger, L. Kegelman, F. Zu, S. Albrecht, N. Koch, T. Kirchartz, M. Saliba, T. Unold, D. Neher, *Energy Environ. Sci.* **2019**, *12*, 2778.
- [88] S. J. Yoon, M. Kuno, P. V. Kamat, *ACS Energy Lett.* **2017**, *2*, 1507.
- [89] A. Ruth, M. C. Brennan, S. Draguta, Y. V. Morozov, M. Zhukovskiy, B. Janko, P. Zapol, M. Kuno, *ACS Energy Lett.* **2018**, *3*, 2321.
- [90] W. Chen, W. Mao, U. Bach, B. Jia, X. Wen, *Small Methods* **2019**, *3*, 1900273.
- [91] R. E. Beal, N. Z. Hagström, J. Barrier, A. Gold-Parker, R. Prasanna, K. A. Bush, D. Passarello, L. T. Schelhas, K. Brüning, C. J. Tassone, H.-G. Steinrück, M. D. McGehee, M. F. Toney, A. F. Nogueira, *Matter* **2020**, *2*, 207.
- [92] Y. Bai, S. Xiao, C. Hu, T. Zhang, X. Meng, H. Lin, Y. Yang, S. Yang, *Adv. Energy Mater.* **2017**, *7*, 1701038.
- [93] K. T. Cho, G. Grancini, Y. Lee, E. Oveisi, J. Ryu, O. Almora, M. Tschumi, P. A. Schouwink, G. Seo, S. Heo, J. Park, J. Jang, S. Paek, G. Garcia-Belmonte, M. K. Nazeeruddin, *Energy Environ. Sci.* **2018**, *11*, 952.
- [94] Y. Liu, S. Akin, L. Pan, R. Uchida, N. Arora, J. V. Milić, A. Hinderhofer, F. Schreiber, A. R. Uhl, S. M. Zakeeruddin, A. Hagfeldt, M. I. Dar, M. Grätzel, *Sci. Adv.* **2019**, *5*, eaaw2543.
- [95] Y. Lin, Y. Bai, Y. Fang, Z. Chen, S. Yang, X. Zheng, S. Tang, Y. Liu, J. Zhao, J. Huang, *J. Phys. Chem. Lett.* **2018**, *9*, 654.
- [96] C. Ortiz-Cervantes, P. Carmona-Monroy, D. Solis-Ibarra, *ChemSusChem* **2019**, *12*, 1560.
- [97] A. Krishna, S. Gottis, M. K. Nazeeruddin, F. Sauvage, *Adv. Funct. Mater.* **2019**, *29*, 1806482.
- [98] Y. Cho, A. M. Soufiani, J. S. Yun, J. Kim, D. S. Lee, J. Seidel, X. Deng, M. A. Green, S. Huang, A. W. Y. Ho-Baillie, *Adv. Energy Mater.* **2018**, *8*, 1703392.
- [99] M. A. Mahmud, T. Duong, Y. Yin, H. T. Pham, D. Walter, J. Peng, Y. Wu, L. Li, H. Shen, N. Wu, N. Mozaffari, G. Andersson, K. R. Catchpole, K. J. Weber, T. P. White, *Adv. Funct. Mater.* **2020**, *30*, 1907962.
- [100] D. Luo, W. Yang, Z. Wang, A. Sadhanala, Q. Hu, R. Su, R. Shivanna, G. F. Trindade, J. F. Watts, Z. Xu, T. Liu, K. Chen, F. Ye, P. Wu, L. Zhao, J. Wu, Y. Tu, Y. Zhang, X. Yang, W. Zhang, R. H. Friend, Q. Gong, H. J. Snaith, R. Zhu, *Science* **2018**, *360*, 1442.
- [101] S. Gharibzadeh, B. Abdollahi Nejad, M. Jakoby, T. Abzieher, D. Hauschild, S. Moghadamzadeh, J. A. Schwenzler, P. Brenner, R. Schmager, A. A. Haghighirad, L. Weinhardt, U. Lemmer, B. S. Richards, I. A. Howard, U. W. Paetzold, *Adv. Energy Mater.* **2019**, *9*, 1803699.
- [102] D. Yao, C. Zhang, S. Zhang, Y. Yang, A. Du, E. Waclawik, X. Yu, G. J. Wilson, H. Wang, *ACS Appl. Mater. Interfaces* **2019**, *11*, 29753.
- [103] C. Chen, Z. Song, C. Xiao, D. Zhao, N. Shrestha, C. Li, G. Yang, F. Yao, X. Zheng, R. J. Ellingson, C.-S. Jiang, M. Al-Jassim, K. Zhu, G. Fang, Y. Yan, *Nano Energy* **2019**, *61*, 141.
- [104] M. A. Green, A. W. Y. Ho-Baillie, *ACS Energy Lett.* **2019**, *4*, 1639.
- [105] H. A. Dewi, H. Wang, J. Li, M. Thway, F. Lin, A. G. Aberle, N. A. Mathews, S. Mhaisalkar, A. Bruno, *Energy Technol.* **2019**, *1901267*, 1901267.
- [106] S. Fantacci, F. De Angelis, M. K. Nazeeruddin, M. Grätzel, *J. Phys. Chem. C* **2011**, *115*, 23126.
- [107] U. B. Cappel, T. Daeneke, U. Bach, *Nano Lett.* **2012**, *12*, 4925.
- [108] I. M. Hossain, Y. Donie, R. Schmager, M. S. Abdelkhalik, M. Rienacker, T. F. Wietler, R. Peibst, A. Karabanov, J. A. Schwenzler, S. Moghadamzadeh, U. Lemmer, B. Richards, G. Gomard, U. Paetzold, *Opt. Express* **2020**, <https://doi.org/10.1364/OE.382253>.
- [109] F. Haase, C. Hollemann, S. Schäfer, A. Merkle, M. Rienacker, J. Krügener, R. Brendel, R. Peibst, *Sol. Energy Mater. Sol. Cells* **2018**, *186*, 184.
- [110] M. Powalla, P. Jackson, W. Witte, D. Hariskos, S. Paetel, C. Tschamber, W. Wischmann, *Sol. Energy Mater. Sol. Cells* **2013**, *119*, 51.
- [111] S. Braunger, L. E. Mundt, C. M. Wolff, M. Mews, C. Rehermann, M. Jošt, A. Tejada, D. Eisenhauer, C. Becker, J. A. Guerra, E. Unger, L. Korte, D. Neher, M. C. Schubert, B. Rech, S. Albrecht, *J. Phys. Chem. C* **2018**, *122*, 17123.
- [112] K. A. Bush, N. Rolston, A. Gold-Parker, S. Manzoor, J. Hausele, Z. J. Yu, J. A. Raiford, R. Cheacharoen, Z. C. Holman, M. F. Toney, R. H. Dauskardt, M. D. McGehee, *ACS Energy Lett.* **2018**, *3*, 1225.